Research Square

Preprints are preliminary reports that have not undergone peer review.
They should not be considered conclusive, used to inform clinical practice,
or referenced by the media as validated information.

No-load field characterisation of a sine-wave-filtered variable-frequency drive feeding an electrical submersible induction motor through a 6000 m cable

Hua Zhang

43929125@qq.com

Bohai Petroleum Equipment Manufacturing Co., Ltd, China National Petroleum Corporation (CNPC)

Guihong Tao

Bohai Petroleum Equipment Manufacturing Co., Ltd, China National Petroleum Corporation (CNPC)

Heng Zhang

Bohai Petroleum Equipment Manufacturing Co., Ltd, China National Petroleum Corporation (CNPC)

Lei Wang

Bohai Petroleum Equipment Manufacturing Co., Ltd, China National Petroleum Corporation (CNPC)

Research Article

Keywords: Electrical submersible pump, Variable-frequency drive, Sine-wave filter, Long cable, Harmonic distortion, Voltage drop

Posted Date: June 30th, 2026

DOI: https://doi.org/10.21203/rs.3.rs-10184577/v1

License: This work is licensed under a Creative Commons Attribution 4.0 International License.
Read Full License

Additional Declarations: No competing interests reported.

No-load field characterisation of a sine-wave-filtered variable-frequency drive feeding an electrical submersible induction motor through a 6000 m cable

Hua Zhang [a],*, Guihong Tao [a], Heng Zhang [a], Lei Wang [a]

[a] *Bohai Petroleum Equipment Manufacturing Co., Ltd., China National Petroleum Corporation (CNPC), Tianjin 300280, China*

* Corresponding author. E-mail: 43929125@qq.com

Abstract

Electrical submersible pumps (ESPs) in deep wells are fed from a surface variable-frequency drive (VFD) through power cables several kilometres long, usually with a sine-wave output filter to protect the motor insulation. Prior power-quality studies of such drives are validated mainly by simulation or reduced-scale laboratory tests; full-scale field data on a real multi-kilometre cable, separating the filter from the cable, are scarce. This paper reports three-phase field measurements on a 45 kW, 946 V submersible induction motor driven, at no load, through a 6000 m armoured cable, at 20, 30 and 40 Hz in three states: VFD direct, VFD with the sine filter, and VFD with the filter and the cable. The sine filter transforms the raw pulse-width-modulated (PWM) voltage (total harmonic distortion, THD, 250-470%, crest factor up to 2.72) into a clean sinusoid (THD 2.4%, crest factor 1.49). The cable then reduces the motor-terminal voltage by 8.3-15.0%; a frequency-dependent distributed-parameter model using the measured cable resistance and inductance reproduces the drop within 3% at 30 and 40 Hz. Notably, the no-load current falls by 29-36%, far more than the voltage; the measured power shows the effective magnetising inductance rises about 30%, indicating magnetic de-saturation—the cable lowers the air-gap flux of the near-saturated motor—as the mechanism. The cable also raises terminal THD to 3.3-3.6%. An LC sine filter is designed and its simulated response compared with the field data. In practice the filter is essential, while the cable voltage drop and de-saturation must be addressed in long-cable ESP design.

Keywords: Electrical submersible pump; Variable-frequency drive; Sine-wave filter; Long cable; Harmonic distortion; Voltage drop

Nomenclature

R_dc	measured cable DC resistance (Ω)
L(f)	measured cable inductance vs frequency (mH)
C	cable shunt capacitance (not measured; bounded range, μF)
Z_c	cable characteristic impedance (Ω)
f_sw	VFD switching frequency (Hz)
f_c	LC filter cutoff frequency (Hz)
L_f, C_f, R_d	filter inductance (mH), capacitance (μF), damping resistance (Ω)
THD_v, THD_i	total harmonic distortion of voltage and current (%, fundamental basis)
X_m, L_m	effective magnetising reactance (Ω) and inductance (mH) at no load
CF	crest factor (peak/RMS)
PF	power factor (no-load)

Abbreviations: ESP, electrical submersible pump; VFD, variable-frequency drive; (S)PWM, (sinusoidal) pulse-width modulation; RMS, root-mean-square.

1 Introduction

Electrical submersible pumps (ESPs) lift a large share of the world's high-rate and deep oil wells [1]. Their reliability is a standing operational concern, and a substantial literature treats ESP failure mechanisms, condition monitoring and diagnostics [2-5]. The arrangement is an unusual one. The induction motor sits at the bottom of the well, its variable-frequency drive (VFD) sits at the surface, and an armoured power cable—often several kilometres

of it—runs between the two. That cable is where the trouble starts. Driven by the fast-switching pulse-width-modulated (PWM) output of the VFD, it behaves as a transmission line, and the familiar power-quality stresses follow: reflected-wave overvoltage and steep dv/dt at the motor terminals, ringing near the cable's natural frequency, extra harmonic heating, and capacitive charging currents [6-9]; the same fast edges also force common-mode and bearing currents that wear the motor bearings [10]. None of this is benign. Field investigations have tied such stresses to premature motor and cable insulation failures in operating oil fields [11-14], and they routinely push the supply past harmonic limits such as IEEE Std 519 [15].

The standard remedy is a sine-wave (LC) output filter at the drive. It reshapes the PWM voltage into something close to a sinusoid, cutting the dv/dt and the total harmonic distortion (THD) that reach the cable and motor [16, 17]; design methods tailored to long-cable ESP drives are by now well established [18, 19]. Filter and cable do not act in isolation, though. The filter output inductance, the cable's distributed inductance and capacitance, and the motor's magnetising inductance together form a network, and that network carries resonances of its own—resonances that can put distortion back and change the current drawn. One point is easy to miss here. Once the filter is fitted and no operator voltage boost is applied, the reflected-wave overvoltage that justified the filter is largely gone, and the questions that matter move downstream, to what the filter and the long cable actually deliver at the motor terminal: the fundamental voltage that arrives, the current the motor then draws, and whatever distortion survives. Answering those needs filter and cable examined together.

Most published analyses of long-cable ESP drives are model-based. High-frequency cable and motor models, together with transmission-line formulations, predict terminal overvoltage and resonance well [7, 8]; more recent work builds integrated VFD-ESP system models that span inverter topologies and capture power-quality as well as torsional behaviour [20, 21], and frequency-domain models of the drive itself have been developed [22, 23]. The validation, however, comes mostly from simulation or reduced-scale laboratory rigs. Even field-based studies tend to pair their measurements with a simulation model rather than isolating the elements experimentally [13]. Full-scale measurements on a real multi-kilometre ESP cable—ones that separate the filter from the cable and report the filtered waveform the motor actually sees—remain scarce. So a few practically important effects stay under-reported: how much voltage is truly lost along a full-length cable, and how the motor current behaves under a filtered, long-cable supply.

This paper addresses that gap with a controlled three-state field test of a Zhongcheng ZC-45 submersible induction motor (45 kW, 946 V) driven, at no load, through a 6000 m armoured cable under V/f control. Measurements taken at the VFD output, the filter output and the motor terminal isolate the contribution of each element. The contributions are: (i) a full-scale field dataset quantifying the sine filter on a real PWM drive (THD, crest factor, waveform) and the 6000 m cable's effect on the filtered signal; (ii) a frequency-dependent circuit model built on the measured cable resistance and inductance that reproduces the field voltage drop, giving field validation rather than simulation-only support; (iii) identification and quantification of a magnetic de-saturation mechanism that explains the pronounced no-load current reduction across the cable—an effect not previously reported for this configuration; and (iv) an LC sine-filter design whose simulated response is set against the field-measured filter. Section 2 describes the system and method, Section 3 reports the measurements, Section 4 analyses them, Section 5 presents the filter design and the simulation-versus-field comparison, and Sections 6-7 discuss and conclude.

2 Test system and method

The motor is a Zhongcheng ZC-45 submersible three-phase induction (asynchronous) motor. It is rated 45 kW, 946 V, 45 A, 50 Hz, and was tested unloaded. Supply comes from a matching in-house Zhongcheng drive of the same 45 kW class, which uses sinusoidal pulse-width modulation at a 2 kHz carrier under constant voltage-to-frequency (V/f) control. The drive feeds the motor optionally through a three-phase sine-wave output filter, and optionally through a 6000 m armoured three-phase cable (single-conductor diameter 5.19 mm). Three states were tested (Fig. 1): State 1, VFD directly to the motor (measured at the VFD output); State 2, VFD through the sine filter to the motor (measured at the filter output); and State 3, VFD through the filter and the 6000 m cable to the motor (measured at the motor terminal). Each state was recorded at 20, 30 and 40 Hz in March 2025.

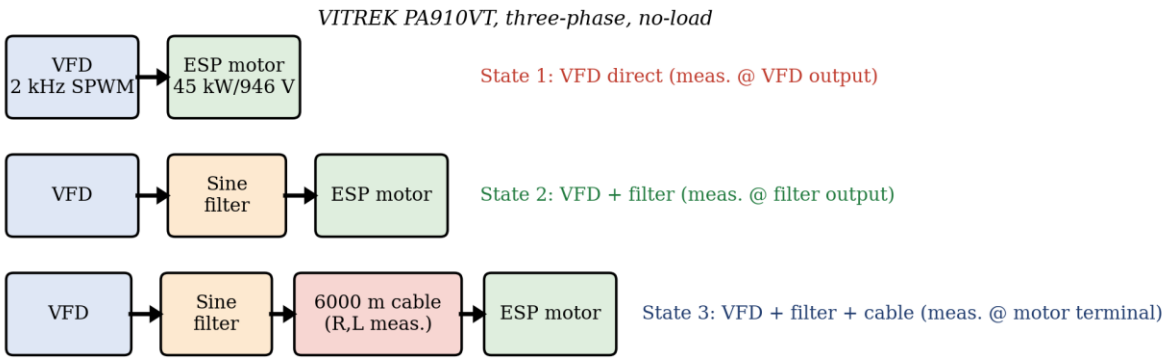


Fig. 1 The three test states. The measurement point moves from the VFD output (States 1, 2) to the motor terminal (State 3) so that the filter and the cable can be characterised separately

Three-phase voltages and currents were recorded with a VITREK PA910VT power-quality analyser [24] (RMS, peak, waveform, harmonic spectrum and THD, vector relationships, and a voltage history for the starting test). The 6000 m cable resistance was measured with a FLUKE 287C multimeter and its inductance with a Tonghui TH2830 digital LCR bridge; Fig. 2 shows the field set-up and a bridge reading of 9.57 mH at 50 Hz. The measured cable parameters are listed in Table 1. The DC resistance approximates the 50 Hz value because the conductor skin depth at power frequency greatly exceeds the conductor radius. The inductance is strongly frequency-dependent—9.57, 6.54 and 4.65 mH at 50 Hz, 100 Hz and 1 kHz—reflecting eddy-current effects in the steel armour; a bridge reading of 3.97 mH at 2 kHz was also recorded. Field conditions did not permit a direct capacitance measurement; the shunt capacitance is therefore bounded by a physically defensible range for an armoured ESP cable, 0.1-0.5 µF/km (0.6-3.0 µF total). As shown in Section 4, this capacitance does not affect any of the three primary results—the filter performance is measured directly, the cable voltage drop depends only on the measured resistance and inductance, and the no-load current reduction is derived from the measured power—so the capacitance enters only the high-frequency resonance discussion (Section 4.3), where the conclusions are shown to hold across the entire range.



Fig. 2 (a) Field test set-up with the 6000 m armoured cable on reels and the VFD/filter cabinet. (b) Cable inductance measured with the TH2830 LCR bridge: 9.57 mH at 50 Hz

Table 1 Measured cable and system parameters. Resistance and inductance were measured (multimeter and LCR bridge); the shunt capacitance was not measured and is bounded by a physical range.

Quantity	Value	Source
Motor	Zhongcheng ZC-45 submersible induction, 45 kW, 946 V, 45 A, 50 Hz	Nameplate
Drive / control	Matching in-house Zhongcheng drive, 2 kHz SPWM, V/f, no load	—
Cable length / conductor	6000 m / 5.19 mm dia.	—

Cable DC resistance	4.85 Ω (0.81 Ω/km)	Measured (multimeter)
Cable inductance @ 50/100/1k Hz	9.57 / 6.54 / 4.65 mH	Measured (LCR bridge)
Cable inductance @ 2 kHz	3.97 mH	Measured (LCR bridge)
Cable shunt capacitance	0.1-0.5 µF/km (0.6-3.0 µF)	Not measured (bounded range)
Characteristic impedance (HF)	39-88 Ω	Derived from C range
Switching frequency	2 kHz	—
Analyser	VITREK PA910VT (3-phase)	—

2.1 Measurement considerations

Three points qualify the measurements and are carried through the analysis. First, each operating point is a single steady-state recording; a formal repeatability study and an instrument uncertainty budget were outside the scope of this field campaign, so the quantitative deviations reported below should be read against the analyser's rated accuracy rather than as exact figures. Second, the harmonic distortion is reported on a fundamental basis (THD_F) [25] up to the analyser's bandwidth of about 5 kHz; because the 2 kHz PWM carrier produces harmonics that extend well beyond 5 kHz, the unfiltered THD values are lower bounds on the true distortion of the raw PWM voltage, whereas the filtered waveforms (dominated by low-order content) and the 2.4-5.4 kHz cable resonance band lie within the measurement bandwidth and are captured reliably. Third, only the cable DC resistance was measured; its high-frequency value, which rises with frequency through skin, proximity and armour effects and which governs the damping of any cable resonance, was not characterised. The voltage-drop analysis (Section 4.1) uses the measured resistance and inductance at the fundamental and is unaffected; the consequence for the high-frequency discussion is noted in Section 4.3.

3 Measured results

3.1 Effect of the sine filter (State 1 vs State 2)

Without the filter (State 1) the VFD output is a raw PWM voltage with very high harmonic content: voltage THD is 251.5%, 468.5% and 349.9% at 20, 30 and 40 Hz, and the crest factor reaches 2.72 (20 Hz), far above the 1.41 of a sinusoid, with peak voltages up to 2025 V. With the sine filter (State 2) the voltage THD collapses to 2.36%, 2.40% and 2.50% and the crest factor falls to about 1.49; the three states are compared in Figs 3-5. The analyser screens in Fig. 6 confirm this directly, showing (a) the raw three-phase PWM voltage at the VFD output and (b) the filtered harmonic spectrum, a clean fundamental with only small low-order residuals (for example a 5th harmonic near 0.66% at 30 Hz). The filter thus removes the switching-band harmonics and lowers the peak voltage, reshaping the PWM into a near-ideal sinusoid. The crest factor and peak voltage are measured directly; the corresponding reduction in dv/dt is inferred from this waveform shaping rather than measured, since the analyser's 5 kHz bandwidth cannot resolve the microsecond switching edges that set the true dv/dt.

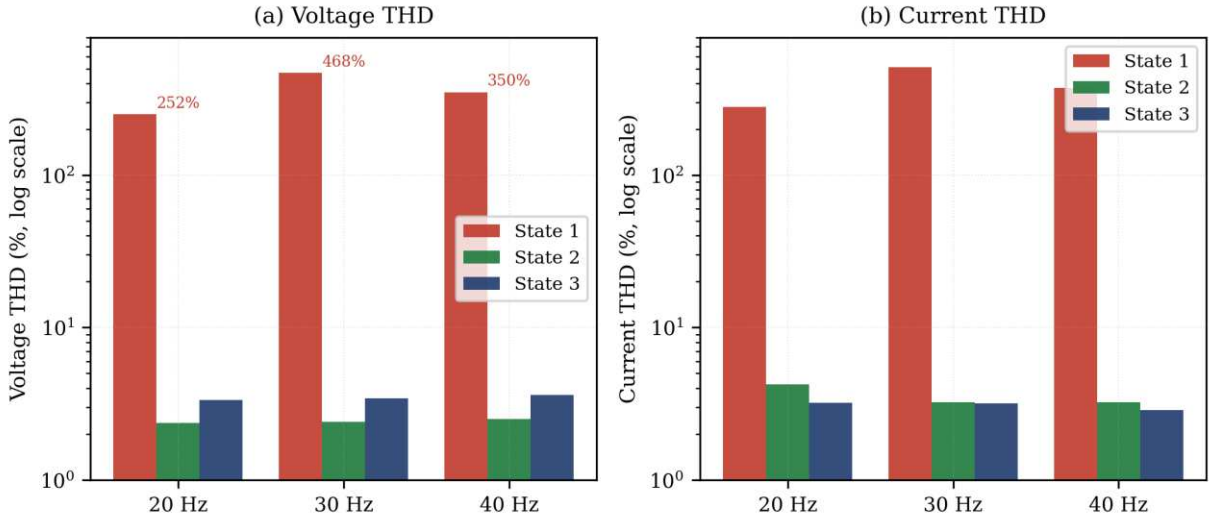


Fig. 3 Measured total harmonic distortion in the three states (log scale). The sine filter (State 2) reduces voltage THD by roughly two orders of magnitude; the cable (State 3) raises it slightly

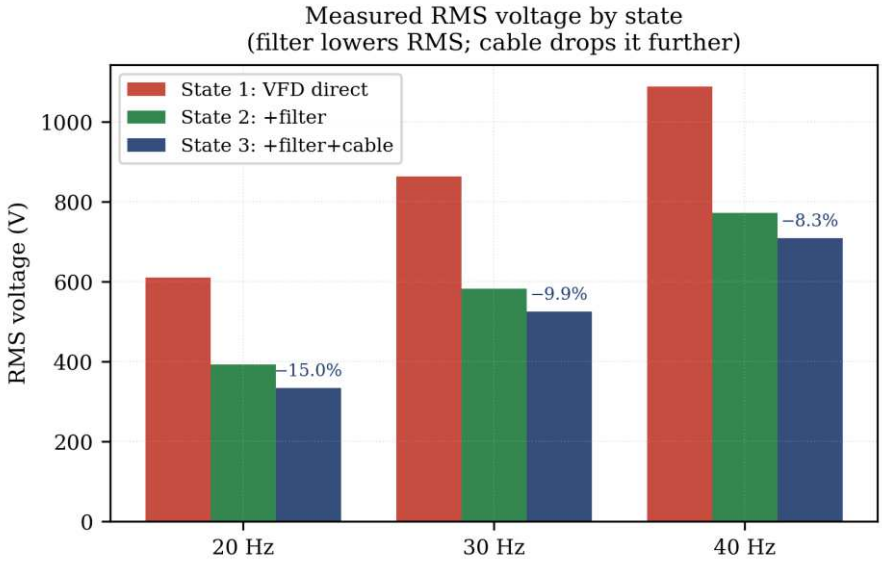


Fig. 4 Measured RMS voltage in the three states. The filter lowers the RMS (removal of harmonic content and filter drop); the 6000 m cable lowers it further by 8-15%

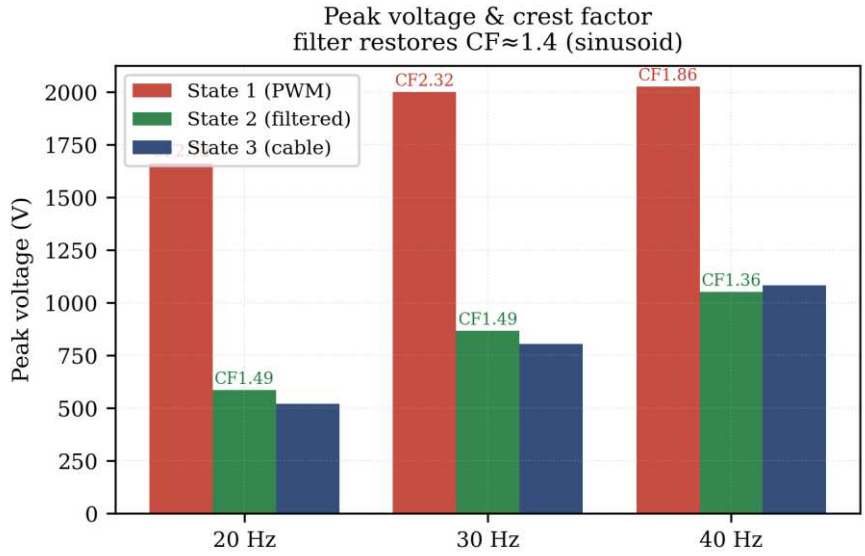


Fig. 5 Measured peak voltage and crest factor (CF). The filter restores a near-sinusoidal CF (≈1.4-1.5) and roughly halves the peak; the implied reduction in dv/dt is inferred from the waveform, not measured directly

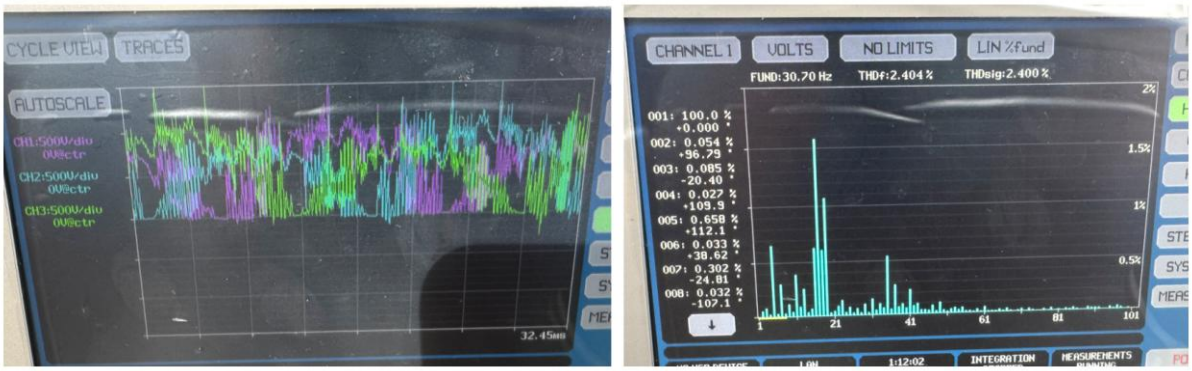


Fig. 6 Measured analyser screens. (a) State 1: raw three-phase PWM voltage at the VFD output. (b) State 2: filtered-output harmonic spectrum at 30.7 Hz, THD 2.40%, dominated by small low-order harmonics

3.2 Effect of the 6000 m cable (State 2 vs State 3)

Adding the cable (State 3, measured at the motor terminal) changes three things. First, the RMS voltage falls by 15.0%, 9.9% and 8.3% at 20, 30 and 40 Hz (Fig. 4). Second, and more strikingly, the no-load current falls by 36.1%, 30.6% and 28.9%, a much larger and oppositely-trending change than a simple charging current would give. Third, the voltage THD rises modestly from about 2.4% to 3.3-3.6%, and the motor-terminal waveform carries a visible high-frequency ripple, with the harmonic spectrum showing a relatively prominent component near the 19th harmonic. The power factor, already low because the unloaded motor is largely magnetising, falls further to 0.23-0.29. Table 2 collects all measured quantities.

Table 2 Measured three-phase quantities (VITREK PA910VT, no load). THD on fundamental basis.

f (Hz)	State	V (V)	V_pk (V)	I (A)	THD_v (%)	THD_i (%)	CF_v	PF
20	1: VFD direct	611.1	1663.3	21.30	251.5	280.2	2.72	—
20	2: +filter	392.6	583.7	20.28	2.36	4.22	1.49	0.316
20	3: +filter+cable	333.8	518.5	12.95	3.33	3.20	1.55	0.23
30	1: VFD direct	863.0	2000	22.29	468.5	510.8	2.32	—
30	2: +filter	582.4	865.5	21.04	2.40	3.24	1.49	0.319
30	3: +filter+cable	524.8	803.9	14.61	3.42	3.17	1.53	0.29
40	1: VFD direct	1089	2025	23.00	349.9	372.6	1.86	—
40	2: +filter	773.1	1049.9	21.75	2.50	3.24	1.36	0.335
40	3: +filter+cable	709.0	1083	15.47	3.62	2.88	1.53	0.29

4 Analysis

4.1 Cable model and voltage drop

The cable is represented as a frequency-dependent distributed-parameter transmission line. Each differential length carries a series impedance $R(f)+j\omega L(f)$ and a shunt admittance $j\omega C$, and the sending-to-receiving relationship follows from the line ABCD matrix, with propagation constant $\gamma=\sqrt{(zy)}$ and characteristic impedance $Z_c=\sqrt{(z/y)}$ for the per-unit-length z and y. The series resistance is taken frequency-dependent (the measured DC value rising with frequency through skin and armour effects); the inductance is the measured L(f); the capacitance is the bounded value of Section 2. This is the model used by recent long-cable ESP studies [8, 20], and it underlies the high-frequency analysis of Section 4.3. At the fundamental, however, the cable is electrically very short—$\gamma\ell$ is below 0.05 at 20-40 Hz—so the line collapses to its lumped series impedance and the shunt branch is negligible. The voltage drop is therefore governed simply by the filter output voltage minus the series-impedance drop. With the measured resistance and frequency-dependent inductance, that impedance is $R_{dc} + j2\pi f L(f)$ (5.0, 5.2 and 5.4

Ω at 20, 30 and 40 Hz). Subtracting the drop carried by the measured motor current from the State 2 voltage predicts the State 3 terminal voltage within +10.1%, +2.9% and +1.3% (Table 3, Fig. 7). The close agreement at 30 and 40 Hz confirms that the bulk of the voltage drop is ordinary series-impedance drop. The larger residual at 20 Hz (+10%) reflects the very low no-load power factor (0.23) at that point, where the predicted terminal voltage is sensitive to small errors in the assumed current phase angle and in the (single-reading) measured quantities; it is not evidence of a capacitive effect (the cable charging current is negligible, below). The neglected cable shunt capacitance does not affect this result: even at the upper bound of the capacitance range (0.5 µF/km), the cable charging current is at most 0.6 A—below 3% of the series voltage drop—so the series-impedance prediction is essentially independent of the unmeasured capacitance.

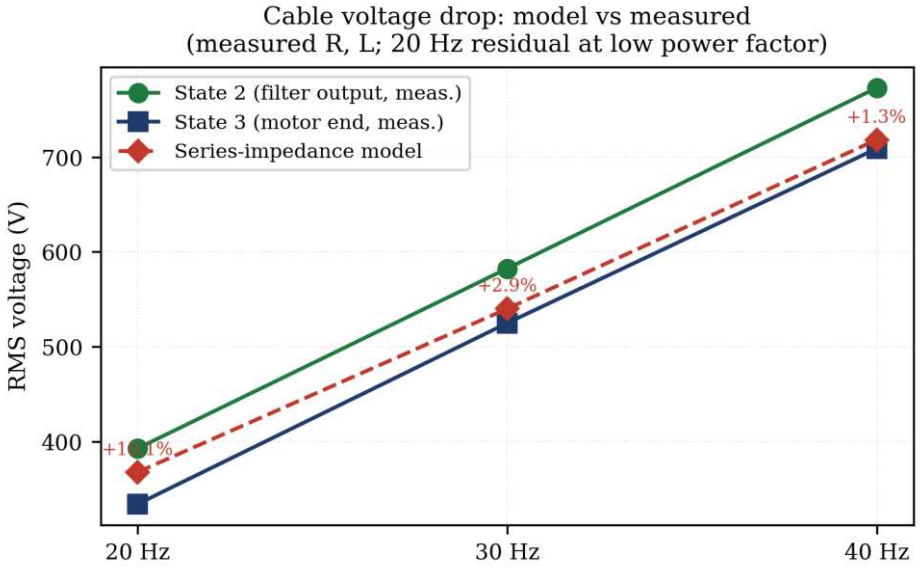


Fig. 7 Cable voltage drop: series-impedance model (measured R and L) versus the measured filter-output (State 2) and motor-terminal (State 3) voltages

Table 3 Cable voltage-drop model (measured R, L) versus measurement.

f (Hz)	|Z_cable| (Ω)	V_pred S3 (V)	V_meas S3 (V)	Dev. (%)
20	5.00	367.5	333.8	+10.1
30	5.17	540.0	524.8	+2.9
40	5.41	718.3	709.0	+1.3

4.2 No-load current reduction: a magnetic de-saturation effect

The 29-36% fall in motor current across the cable (Fig. 8) is the most distinctive observation, and it is disproportionate—far larger than the 8-15% voltage drop. A lumped cable charging current ($V \cdot 2\pi f \cdot C$), evaluated even at the upper bound of the capacitance range, is at most 0.6 A and would increase with frequency, whereas the measured reduction is several amperes and is largest at 20 Hz; simple capacitive charging therefore cannot explain it for any capacitance in the physical range. Resolving the measured terminal quantities into real and reactive power identifies the mechanism. At no load the motor is dominated by its magnetising branch, so the per-phase reactive power defines an effective magnetising reactance $X_m = V^2/Q$ and inductance $L_m = X_m/2\pi f$.

Table 4 lists these values. From State 2 to State 3 the effective magnetising inductance rises by 27-30% (for example 94→122 mH at 20 Hz). The cause is magnetic saturation. A flux-dependent magnetising inductance is a standard feature of induction-machine models [26-28]; what is new here is seeing it driven by the cable voltage drop in a field ESP installation. Under V/f control the unloaded motor runs slightly above its rated flux at the filter output—the measured V/f is 19.3-19.6 V/Hz against a rated 18.9 V/Hz—placing it near the knee of its magnetisation curve (Fig. 9). The no-load data make this concrete. Extrapolated to rated flux, the magnetising reactance is about 28 Ω at 50 Hz, drawing roughly 19 A; that is some 43% of the 45 A rating, a high magnetising fraction typical of slender submersible motors and a clear sign of operation close to saturation. The cable voltage

drop lowers the air-gap flux by 8-15%, moving the operating point down the curve into a less-saturated region of higher inductance. Since the magnetising current is $I_m = V/(2\pi f L_m)$, the simultaneous fall in voltage and rise in inductance gives a current ratio of about $0.85/1.30 \approx 0.65$ at 20 Hz—a 35% reduction—consistent with the measured 36% (this is an internal consistency check, since the inductance is itself extracted from the measured currents, rather than an independent prediction). The 30 and 40 Hz reductions follow the same way, and the largest drop at 20 Hz follows directly from the largest flux reduction there (Table 4).

The robust, measurement-based finding here is the 27-30% rise in the effective magnetising inductance from State 2 to State 3; magnetic de-saturation is the physical interpretation, supported by the unloaded motor's V/f sitting above its rated value. This interpretation should, however, be regarded as identified rather than independently proven: it rests on single readings and on the terminal reactance, without a measured magnetisation curve or a separated equivalent circuit, so secondary contributions (for example temperature, the small cable shunt current, or measurement scatter) cannot be fully excluded. The mechanism complements rather than replaces the cable capacitance effects, which act at higher frequency and govern the small THD increase of Section 4.3. It is unloaded—under load, where the current is larger and more resistive, the relative weight of this effect is smaller. A loaded test and an independently measured magnetisation curve would confirm and quantify it.

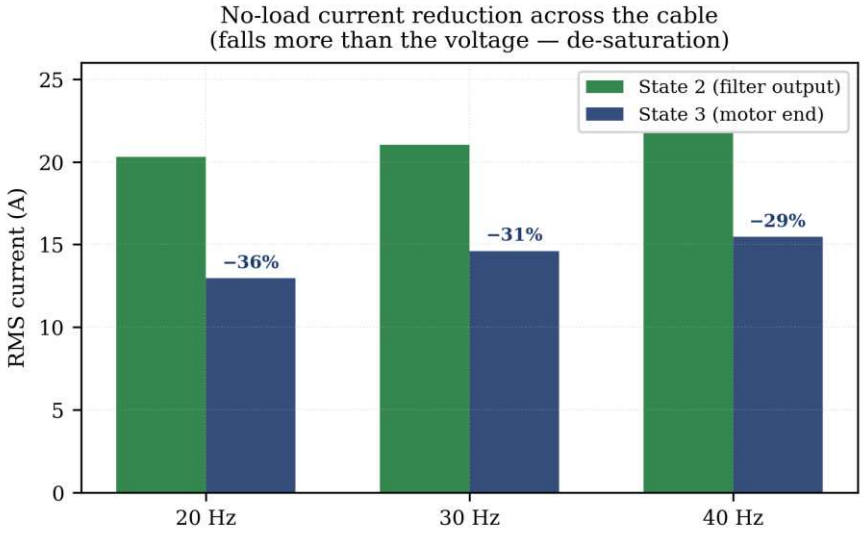


Fig. 8 Measured no-load current at the filter output (State 2) and the motor terminal (State 3). The reduction is largest at low frequency and exceeds the voltage drop

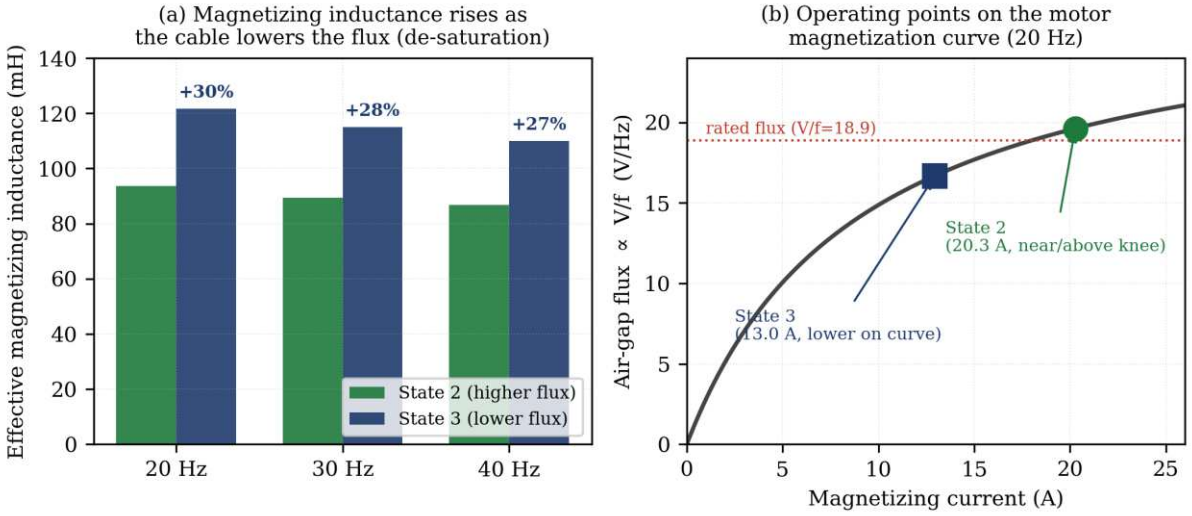


Fig. 9 Magnetic de-saturation indicated by the measurements. (a) The effective magnetising inductance, from the measured reactive power, rises 27-30% from State 2 to State 3. (b) The cable voltage drop moves the operating point down the magnetisation curve to a less-saturated, higher-inductance region

Table 4 No-load magnetising quantities from the measured reactive power, and the resulting current ratio. $Q = \sqrt{3}\cdot V\cdot I\cdot \sin\varphi$; $X_m = (V/\sqrt{3})^2/(Q/3)$; $L_m = X_m/2\pi f$.

f (Hz)	L_m State 2 (mH)	L_m State 3 (mH)	L_m ratio	I3/I2 (model)	I3/I2 (meas.)
20	93.7	121.7	1.30	0.655	0.639
30	89.5	115.0	1.29	0.701	0.694
40	86.7	110.0	1.27	0.722	0.711

4.3 High-frequency ripple and cable resonance

The small high-frequency ripple that the cable adds to the otherwise clean filtered voltage is a transmission-line effect, and the distributed model captures it where a lumped element cannot. At a few kilohertz the 6000 m cable is no longer electrically short: it approaches a quarter-wavelength, so it supports standing-wave resonances. The first of these is a quarter-wave resonance. Evaluating the distributed transfer function over the full capacitance range places it between about 2.4 and 5.4 kHz (Fig. 10); the analytic estimate $v/4\ell$, with a propagation velocity of roughly 0.26c, agrees. This band sits well above the filter cutoff and the low-order harmonics, but it overlaps the switching frequency and its multiples. Residual switching-band content that survives the filter is therefore shaped by the cable response, and the terminal THD rises modestly—from about 2.4% to 3.3-3.6%. The mechanism does not depend on the exact capacitance: only the precise resonance frequency does, while the band stays in the low kilohertz for any value in the physical range. How sharp the resonance is depends on the high-frequency resistance, and only the DC value was measured. A skin-effect calculation puts the conductor resistance near the resonance at roughly 1.2 times the DC value—a lower bound, since the steel armour adds eddy-current losses, as the measured 58% fall in inductance from 50 Hz to 2 kHz already implies. The true high-frequency resistance is thus higher, and the resonance is comparatively well damped. That fits what is observed: a gentle one-point rise in THD, not a sharp resonant spike.

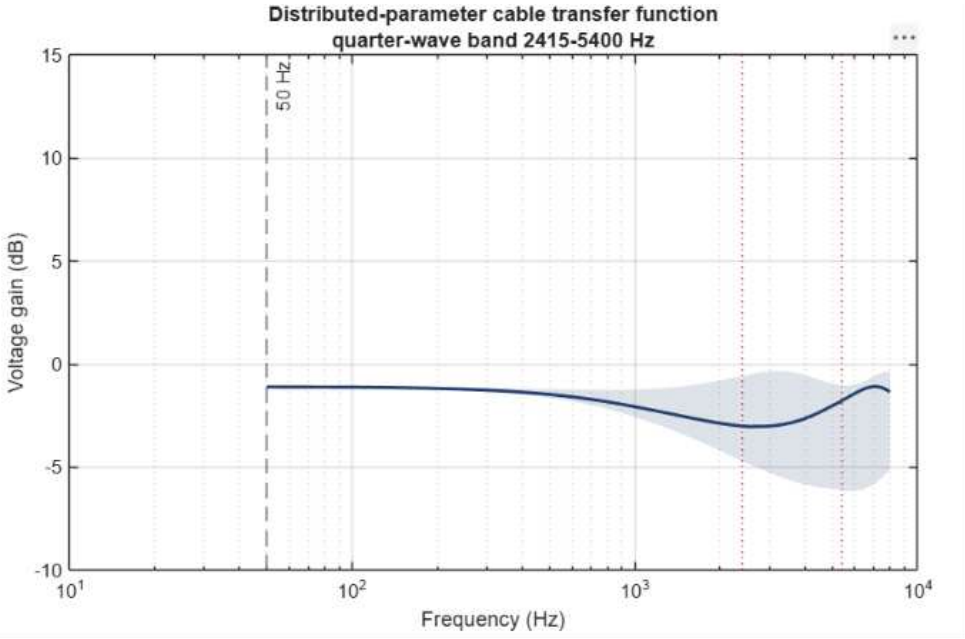


Fig. 10 Cable voltage transfer function from the frequency-dependent distributed-parameter model (measured R, L; capacitance swept over 0.1-0.5 µF/km). The quarter-wave resonance band lies at ≈2.4-5.4 kHz for any capacitance, overlapping the switching harmonics; the high-frequency resistance damps it, consistent with the small measured THD rise

5 LC sine-wave filter: design and comparison with the field test

The field test used a sine filter whose internal parameters were not documented. To provide a transparent, reproducible design basis—and to compare a simulated filter against the measured one—an LC sine-wave filter is designed here from first principles and simulated.

5.1 Design procedure

Following standard inverter-filter practice [29], the filter is a series inductor with a damped shunt capacitor on each phase at the drive output. The design steps are: (1) place the cutoff frequency at the geometric mean of the maximum fundamental and the switching frequency, $f_c = \sqrt{(50 \times 2000)} \approx 316$ Hz, well above the fundamental and about a decade below the 2 kHz carrier; (2) choose a filter characteristic impedance between the motor fundamental impedance (≈12 Ω) and the cable characteristic impedance, here 18 Ω; (3) obtain $L_f = Z_f/(2\pi f_c)$ and $C_f = 1/(2\pi f_c Z_f)$; (4) round to engineering values $L_f = 7.5$ mH and $C_f = 33$ µF (actual $f_c = 320$ Hz); and (5) add a series damping resistor $R_d = 2.7$ Ω to limit the filter quality factor and avoid an under-damped peak. The parameters are summarised in Table 5.

Table 5 Designed LC sine-wave filter (per phase).

Parameter	Value
Cutoff frequency f_c	320 Hz
Inductance L_f	7.5 mH
Capacitance C_f	33 µF
Damping resistance R_d	2.7 Ω
Attenuation at $f_{sw} = 2$ kHz	≈ −29 dB

5.2 Frequency response and time-domain simulation

The designed filter's frequency response (Fig. 11) passes the fundamental with about 0.2 dB insertion loss and attenuates the 2 kHz switching component by roughly 29 dB, with further attenuation above. This is the quantitative basis for the large THD reduction: the switching-band harmonics that dominate the raw PWM spectrum are suppressed by more than a factor of twenty. A time-domain simulation of the filter driven by a 2 kHz SPWM source (Fig. 12) reproduces the expected action, converting the pulsed input into a smooth fundamental sinusoid.

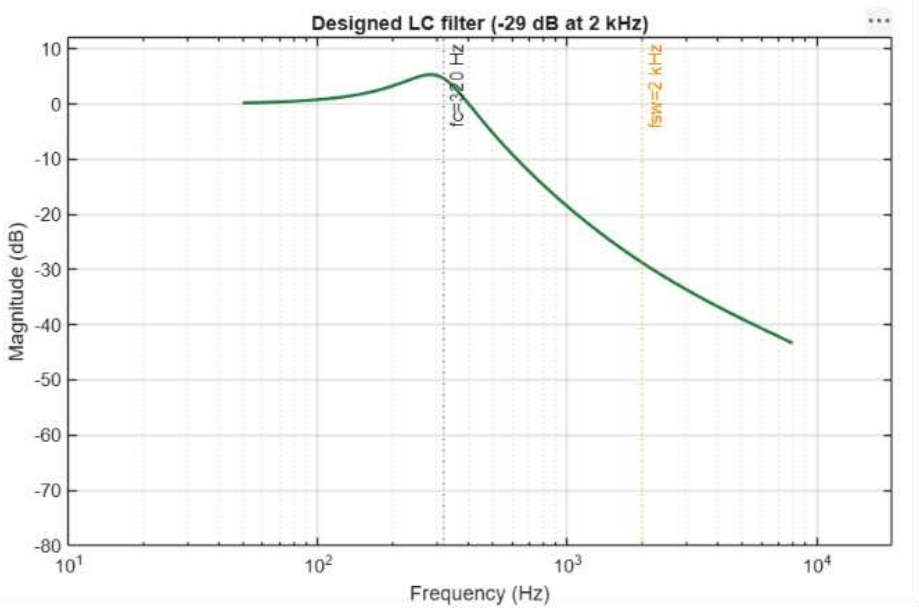


Fig. 11 Designed LC filter frequency response. About 29 dB attenuation at 2 kHz with negligible insertion at the fundamental

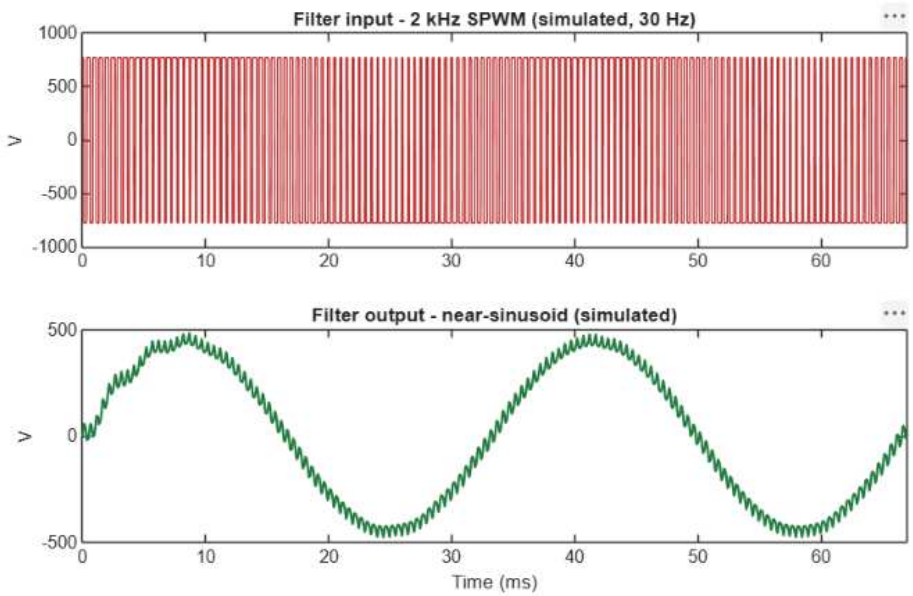


Fig. 12 Time-domain simulation of the designed filter at 30 Hz (model output): (a) PWM input, (b) filtered sinusoidal output

5.3 Comparison with the field measurement

The designed and simulated filter can now be set against the field-tested one. The design predicts strong suppression of the switching-band harmonics (≈29 dB at 2 kHz); the field measurement independently confirms that the installed filter reduces the voltage THD from 250-470% to 2.4% and restores a crest factor of 1.49 against the ideal 1.41. Both the simulated and the measured filtered voltages are clean fundamental sinusoids. The two therefore agree on the filter's essential action, which validates the design methodology and the simulation model and provides a basis for future filter optimisation. A quantitative caveat is that the simplified single-phase time-domain model retains more low-order residual distortion than the three-phase field measurement, in which triplen harmonics cancel in the line voltage; the measured 2.4% is the more reliable figure, and the simulation is best read as confirming the mechanism and the waveform rather than predicting the THD to the tenth of a percent.

6 Discussion

The three-state field test yields a clear engineering picture. The sine filter is indispensable: it converts a severely distorted PWM voltage into a near-ideal sinusoid, cutting THD by two orders of magnitude and roughly halving the peak voltage, which is expected to reduce the dv/dt and reflected-wave stress on the cable and motor insulation, although the dv/dt itself was below the analyser bandwidth and is inferred rather than measured. The 6000 m cable then imposes two issues that the filter does not solve: a fundamental voltage drop of 8-15%, which under-excites the motor and must be compensated (for example by a modest, deliberate increase of the V/f setpoint sized to the measured series impedance, or by a tap change), and a no-load current reduction that, as Section 4.2 shows, is a magnetic de-saturation effect—the voltage drop lowers the air-gap flux of the near-saturated unloaded motor—accompanied by a high-frequency ripple from the cable's own resonance.

These results complement the model-based literature with full-scale field evidence. Integrated VFD-ESP system models and high-frequency cable/motor models reproduce overvoltage and resonance and have been validated by simulation and reduced-scale laboratory tests [8, 20, 21]; the present measurements extend that body of work to a real 6000 m cable and, by separating the filter from the cable, quantify the filtered waveform actually delivered to the motor. The de-saturation mechanism for the no-load current, obtained here directly from field measurements, is to the authors' knowledge not reported in those studies and is a candidate effect for inclusion in future ESP system models.

6.1 Projected behaviour under load

The test was unloaded, so the loaded case deserves comment. What follows is a first-order projection from the measured cable parameters and the motor nameplate—not a measurement. It is meant to indicate trends, and the

compensation that loaded operation would demand. Three things change; one does not. The filter is the one that does not. It sits at the drive output, ahead of both the cable and the load, so its harmonic suppression is essentially load-independent and the filtered THD should stay near the measured 2.4%. The voltage drop, by contrast, grows. At rated load the motor draws up to 45 A, roughly 2.2 times the no-load current, and the series-impedance drop scales with current; the uncompensated drop would rise from the measured 8-15% to about 27% at rated frequency, and higher still lower down—past 50% near 20 Hz. Operator boost or a step-up transformer is therefore mandatory under load, which is exactly the compensation that the no-load test, run without boost, could omit. The de-saturation effect weakens. Its size is set by the magnetising current, and that current is only about 43% of the rated current; under load the resistive rotor current dominates, so the roughly 30% magnetising reduction becomes a change of only about 13% in the total current. The striking no-load current drop is thus largely a no-load phenomenon. The cable resonance, finally, is a network property: its low-kHz band is unchanged, and the added load resistance damps it further, so the high-frequency degradation should be no worse than that measured here.

6.2 Limitations and outlook

Several limitations qualify these results. (i) The test was conducted at no load. The loaded behaviour projected in Section 6.1 is model-based and awaits a loaded field test for confirmation. (ii) Each operating point is a single reading without a repeatability or uncertainty budget. (iii) The cable resistance and inductance were measured (the inductance across frequency); the shunt capacitance could not be measured in the field and was instead bounded by a physical range, over which all conclusions were shown to be robust—the three primary results are independent of it and the high-frequency resonance remains in the low-kHz band for any value in the range—so only the precise resonance frequency, of secondary importance, is left uncertain. (iv) The internal parameters of the installed sine filter were not available, so the filter modelled here is a representative design rather than the exact unit; the comparison validates the methodology, not specific component values. (v) The simulation is single-phase and therefore conservative on residual THD. Addressing these—loaded tests with an uncertainty budget, a direct capacitance measurement to pin the exact resonance frequency, the installed filter parameters, and a three-phase model—would turn this first-order field study into a fully quantitative one.

7 Conclusions

Three-phase field measurements of a 45 kW, 946 V submersible induction motor driven, at no load, through a 6000 m armoured cable, in three controlled states, establish the following. (1) A sine-wave output filter transforms the raw PWM voltage (THD 250-470%, crest factor up to 2.72) into a clean sinusoid (THD 2.4%, crest factor 1.49), confirming its value for dv/dt and insulation protection. (2) The 6000 m cable reduces the motor-terminal voltage by 8.3-15.0%; a frequency-dependent cable model using the measured resistance (4.85 Ω) and inductance (9.57 mH at 50 Hz) reproduces the drop within 3% at 30 and 40 Hz. (3) The no-load motor current falls by 29-36% across the cable—far more than the 8-15% voltage drop—because the voltage drop de-saturates the unloaded motor: decomposing the measured power shows the effective magnetising inductance rises about 30%, so the magnetising current falls faster than the voltage. This is the test's most noteworthy finding for long-cable ESP design. (4) The cable re-introduces a small high-frequency ripple, raising terminal THD to 3.3-3.6%. An LC sine filter designed and simulated here reproduces the field-observed suppression (≈29 dB at the switching frequency) and waveform, validating the design methodology. In practice the sine filter is essential for waveform quality, while the cable voltage drop must be compensated and the low-kHz cable resonance accounted for. A loaded, instrumented field test is the natural next step.

Statements and Declarations

Author contributions

Conceptualization: Hua Zhang; Methodology: Hua Zhang; Investigation: Hua Zhang, Guihong Tao, Heng Zhang; Formal analysis: Guihong Tao; Visualization: Guihong Tao; Data curation: Heng Zhang; Validation: Heng Zhang; Resources and software: Lei Wang; Writing – original draft: Hua Zhang; Writing – review and editing: Heng Zhang. All authors read and approved the final manuscript.

Competing interests

The authors declare that they have no known competing financial interests or personal relationships that could have appeared to influence the work reported in this paper.

Funding

The authors did not receive support from any organization for the submitted work.

Use of generative AI tools

Not applicable. The authors declare that no generative AI tools or AI-assisted technologies were used in the preparation of this manuscript.

Data availability

The data supporting the findings of this study are available from the corresponding author upon reasonable request.

Acknowledgments

The authors thank colleagues at the Bohai Petroleum Equipment Research Institute (CNPC) for support with the field test.

References

[1] Takacs G (2017) Electrical submersible pumps manual: design, operations, and maintenance, 2nd edn. Gulf Professional Publishing (Elsevier), Cambridge

[2] Fakher S, Khlaifat A, Hossain ME, Nameer H (2021) Rigorous review of electrical submersible pump failure mechanisms and their mitigation measures. J Pet Explor Prod Technol 11(10):3799-3814

[3] De Moura Fonseca DA, Salazar AO, Villarreal ERL, Echaiz Espinoza GA, Leite ACQB (2021) Downhole telemetry systems to monitor electric submersible pump parameters in oil wells. IEEE Access 9:12824-12839

[4] Li L, Hua C, Xu X (2018) Condition monitoring and fault diagnosis of electric submersible pump based on wellhead electrical parameters and production parameters. Syst Sci Control Eng 6(3):253-261

[5] Wei Q et al (2024) Research on early warning model of electric submersible pump wells failure based on the fusion of physical constraints and data-driven approach. Geoenergy Sci Eng 233:212489

[6] Persson E (1992) Transient effects in application of PWM inverters to induction motors. IEEE Trans Ind Appl 28(5):1095-1101

[7] Kerkman RJ, Leggate D, Skibinski GL (1997) Interaction of drive modulation and cable parameters on AC motor transients. IEEE Trans Ind Appl 33(3):722-731

[8] Moreira AF, Lipo TA, Venkataramanan G, Bernet S (2002) High-frequency modeling for cable and induction motor overvoltage studies in long cable drives. IEEE Trans Ind Appl 38(5):1297-1306

[9] Narayanasamy B, Sathyanarayanan A, Deshpande A, Luo F (2020) Reflected wave phenomenon in SiC motor drives: consequences, boundaries, and mitigation. IEEE Trans Power Electron 35(10):10629-10642

[10] Akagi H, Doumoto T (2004) An approach to eliminating high-frequency shaft voltage and ground leakage current from an inverter-driven motor. IEEE Trans Ind Appl 40(4):1162-1169

[11] Pragale RO, Shipp DD (2017) Investigation of premature ESP failures and oil field harmonic analysis. IEEE Trans Ind Appl 53(4):3175-3181

[12] Abdelazim Mellik T, Shipp DD, Dionise TJ (2019) Reducing electrical submersible pump downtime by mitigation of VSD output power quality problems. In: Proc IEEE Petroleum and Chemical Industry Technical Conference (PCIC), pp 485-494

[13] Liang X, El-Kadri A (2019) Operational parameters affecting harmonic resonance in electrical submersible pump systems. IEEE Can J Electr Comput Eng 42(3):183-197

[14] Rabbi SF, Kahnamouei JT, Liang X, Yang J (2020) Shaft failure analysis in soft-starter fed electrical submersible pump systems. IEEE Open J Ind Appl 1:1-10

[15] IEEE (2014) IEEE Std 519-2014: IEEE recommended practice and requirements for harmonic control in electric power systems. IEEE, Piscataway

[16] von Jouanne A, Enjeti PN (1997) Design considerations for an inverter output filter to mitigate the effects of long motor leads in ASD applications. IEEE Trans Ind Appl 33(5):1138-1145

[17] Rendusara DA, Enjeti PN (1998) An improved inverter output filter configuration reduces common- and differential-mode dv/dt at the motor terminals in PWM drive systems. IEEE Trans Power Electron 13(6):1135-1143

[18] Liang X, Kar NC, Liu J (2015) Load filter design method for medium-voltage drive applications in electrical submersible pump systems. IEEE Trans Ind Appl 51(3):2017-2029

[19] Mirza AB, Vala SS, Choksi K, Luo F (2024) Simplified analytical modeling of reflected wave transients in cable-connected VSI-based motor drives with output reactor. IEEE Trans Power Electron 39(10):11986-11990

[20] Lingom PM, Song-Manguelle J, Doumbia ML, Flesch RCC, Jin T (2022) Electrical submersible pumps: a system modeling approach for power quality analysis with variable frequency drives. IEEE Trans Power Electron 37(6):7039-7054. https://doi.org/10.1109/TPEL.2021.3133758

[21] Lingom PM, Song-Manguelle J, Betoka-Onyama SP, Nyobe-Yome J-M, Doumbia ML (2023) A power quality assessment of electric submersible pumps fed by variable frequency drives under normal and failure modes. Energies 16(13):5121. https://doi.org/10.3390/en16135121

[22] Yadav J, Vasudevan K, Meyer J, Kumar D (2022) Frequency coupling matrix model of a three-phase variable frequency drive. IEEE Trans Ind Appl 58(3):3652-3663

[23] Zhang Y, Li YW (2015) Investigation and suppression of harmonics interaction in high-power PWM current-source motor drives. IEEE Trans Power Electron 30(2):668-679

[24] Vitrek LLC (n.d.) VITREK PA900/PA910 series precision power analyzer, user manual. Vitrek LLC, Poway

[25] Arrillaga J, Watson NR (2003) Power system harmonics, 2nd edn. Wiley, Chichester

[26] Sudhoff SD, Aliprantis DC, Kuhn BT, Chapman PL (2002) An induction machine model for predicting inverter-machine interaction. IEEE Trans Energy Convers 17(2):203-210

[27] Masadeh MA, Amitkumar KS, Pillay P (2018) Power electronic converter-based induction motor emulator including main and leakage flux saturation. IEEE Trans Transp Electrif 4(2):483-493

[28] Levi E (1994) Applications of the current state space model in analyses of saturated induction machines. Electr Power Syst Res 31(3):203-216

[29] Mohan N, Undeland TM, Robbins WP (2003) Power electronics: converters, applications, and design, 3rd edn. Wiley, New York